



CT-Based Radiomics Signature for Preoperative Prediction of Coagulative Necrosis in Clear Cell Renal Cell Carcinoma

Kai Xu, MD¹, Lin Liu, MD, PhD¹, Wenhui Li, PhD², Xiaoqing Sun, MD¹, Tongxu Shen, MD¹, Feng Pan, MD¹, Yuqing Jiang, MD¹, Yan Guo, MD³, Lei Ding, MD¹, Mengchao Zhang, MD, PhD¹

¹Department of Radiology, China-Japan Union Hospital of Jilin University, Changchun, China; ²College of Computer Science and Technology, Jilin University, Changchun, China; ³Life Sciences, GE Healthcare, China, Shenyang, China

Objective: The presence of coagulative necrosis (CN) in clear cell renal cell carcinoma (ccRCC) indicates a poor prognosis, while the absence of CN indicates a good prognosis. The purpose of this study was to build and validate a radiomics signature based on preoperative CT imaging data to estimate CN status in ccRCC.

Materials and Methods: Altogether, 105 patients with pathologically confirmed ccRCC were retrospectively enrolled in this study and then divided into training (n = 72) and validation (n = 33) sets. Thereafter, 385 radiomics features were extracted from the three-dimensional volumes of interest of each tumor, and 10 traditional features were assessed by two experienced radiologists using triple-phase CT-enhanced images. A multivariate logistic regression algorithm was used to build the radiomics score and traditional predictors in the training set, and their performance was assessed and then tested in the validation set. The radiomics signature to distinguish CN status was then developed by incorporating the radiomics score and the selected traditional predictors. The receiver operating characteristic (ROC) curve was plotted to evaluate the predictive performance.

Results: The area under the ROC curve (AUC) of the radiomics score, which consisted of 7 radiomics features, was 0.855 in the training set and 0.885 in the validation set. The AUC of the traditional predictor, which consisted of 2 traditional features, was 0.843 in the training set and 0.858 in the validation set. The radiomics signature showed the best performance with an AUC of 0.942 in the training set, which was then confirmed with an AUC of 0.969 in the validation set.

Conclusion: The CT-based radiomics signature that incorporated radiomics and traditional features has the potential to be used as a non-invasive tool for preoperative prediction of CN in ccRCC.

Keywords: Coagulative necrosis; Clear cell renal cell carcinoma; CT; Radiomics

INTRODUCTION

Renal cell carcinoma (RCC) is the most common primary malignancy of the kidney, accounting for approximately

85–90% of renal malignancies. Clear cell renal cell carcinoma (ccRCC) is the most common subtype of RCC, accounting for approximately 70% of the cases (1). With the increased health awareness among people and the development of advanced examination methods, the proportion of RCC cases that are being incidentally detected is gradually increasing (2-5). Among incidental RCCs, ccRCC is a common pathological type and has a higher risk of a poor prognosis (6, 7); therefore, it has received more attention in clinical practice. Radiofrequency treatment or cryoablation have recently become options for the treatment of renal cancer and are suitable for tumors with good prognosis (8, 9). Therefore, there is an urgent need for preoperative assessment of the prognosis of ccRCC. Histological coagulative necrosis (CN) has been widely recognized as an important independent prognostic factor for ccRCC (7, 10-13). Studies have shown that the 10-year

Received: August 31, 2019 **Revised:** December 9, 2019

Accepted: January 27, 2020

This study was supported by the science and Technology Development Plant of Jilin Province (No.20180101015JC), the research grant from the Jilin Province Science and Technology Development Plan Project (NO.20190303182SF).

Corresponding author: Mengchao Zhang, MD, PhD, Department of Radiology, China-Japan Union Hospital of Jilin University, NO. 126 Xiantai Street, Changchun 130033, China.

• Tel: (86) 15948705198 • Fax: (86) 431-849957

• E-mail: zhangmengchao@jlu.edu.cn

This is an Open Access article distributed under the terms of the Creative Commons Attribution Non-Commercial License (<https://creativecommons.org/licenses/by-nc/4.0>) which permits unrestricted non-commercial use, distribution, and reproduction in any medium, provided the original work is properly cited.

cancer-specific survival in patients showing CN in ccRCC tumors is 29.2%, while the corresponding value in those without necrosis is as high as 77.6% (11). Moreover, for ccRCC, the risk ratio of death in patients with CN and non-necrosis in the tumor is 5.27 (11). Therefore, prediction of the presence or absence of CN within the tumor before surgery is a very important factor influencing the choice of treatment strategy for RCCs. Although needle biopsy is an effective method for obtaining pathological findings before surgery, because of tumor heterogeneity, needle biopsy does not yield convincing results related to CN (14). Moreover, as an invasive examination, this technique can cause a variety of complications (15). Therefore, it is worth exploring whether noninvasive methods can be used to predict CN in ccRCC accurately.

Previous studies have shown that traditional image features, such as enhancement characteristics, could provide valuable predictive information for identifying benign and malignant tumors, tumor subtypes, and tumor grades in RCC (16, 17). Nowadays, with the development of radiomics technology, radiomics methods that translate medical imaging data into high-dimension data can also be used as non-invasive biomarkers for prognosis or prediction (18-21). However, it remains unclear whether it is possible to predict the presence or absence of CN in ccRCC tumors by using radiomics features and traditional features based on CT images. Moreover, the types of features that could yield a higher prediction accuracy are unknown.

Therefore, the purpose of this study was to build and validate a radiomics score and a traditional predictor based on CT imaging for prediction of the CN status in ccRCC. Moreover, we developed an inclusive radiomics signature incorporating the radiomics score and traditional predictors for preoperative estimation of the CN status in ccRCC patients.

MATERIALS AND METHODS

Patients

The retrospective study was approved by the Ethics Review Committee of our hospital. The requirement for informed consent was waived because CT image acquisition is part of a routine non-invasive examination protocol for suspected RCC patients.

Between March 2013 and March 2019, 105 patients with ccRCC underwent surgical resection in our hospital; the obtained pathological results were collected in this study.

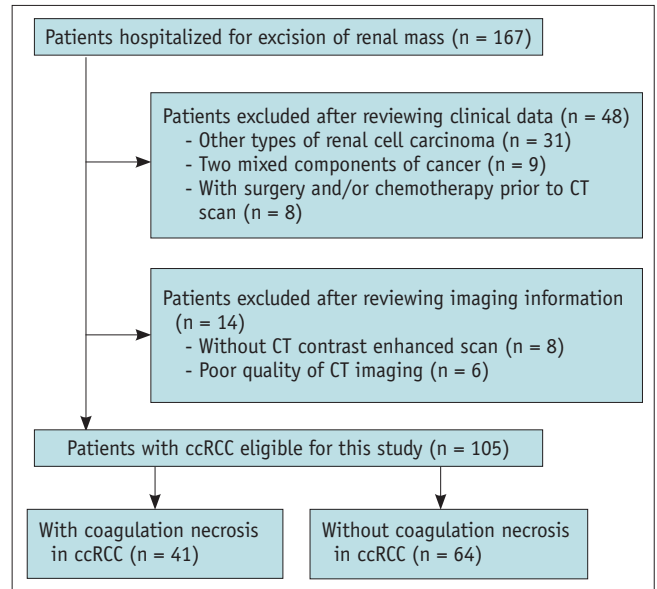


Fig. 1. Flow chart of patient recruitment with inclusion and exclusion criteria. ccRCC = clear cell renal cell carcinoma

Patient inclusion/exclusion criteria are presented in Figure 1. Furthermore, a renal mass was obtained from each patient. After strict screening of the enrolled patients, 105 patients were included in the study.

Sample Size Consideration

Based on sample size calculation methods in clinical research (22) introduced by Shein-Chung Chow, Ph.D., we estimated the validation sample size that was sufficiently independent to test whether our model was robust and efficient.

First, considering the two groups to be A and B, μ represents the mean value of the average radiomics score for each group, with the hypotheses of interest being as follows:

$$H_0: \mu_A - \mu_B = 0$$

$$H_1: \mu_A - \mu_B \neq 0$$

The sample size and power are calculated respectively as follows:

$$N_A = \left(\frac{n_A + n_B}{n_B} \right) \left(\sigma \frac{Z_{1-\alpha/2} + Z_{1-\beta}}{\mu_A + \mu_B} \right)^2$$

$$N_B = \left(\frac{n_A + n_B}{n_A} \right) \left(\sigma \frac{Z_{1-\alpha/2} + Z_{1-\beta}}{\mu_A + \mu_B} \right)^2$$

$$1 - \beta = \Phi(z - Z_{1-\alpha/2}) + \Phi(-z - Z_{1-\alpha/2}), z = \frac{\mu_A - \mu_B}{\sigma \sqrt{\frac{1}{n_A} + \frac{1}{n_B}}}$$

Where n is the sample size in the training group and N is the sample size for the validation group, Φ is the standard normal distribution function, α is the type I error, β is the type II error, $1 - \beta$ is the power, and σ^2 is the variance of the covariate.

In our study, the sample sizes in the training groups were $n_A = 28$ and $n_B = 44$ with means of $\mu_A = -2.086$ and $\mu_B = 0.643$, respectively, and with a variance of $\sigma^2 = 3.3508$. Therefore, the minimum number of validation samples was 15 (without CN) and 10 (with CN) in the two groups with the desired two-sided significance level of $\alpha = 0.05$ and power of $1 - \beta = 95\%$. In our study, the validation set included 20 cases without CN and 13 cases with CN in the two groups, respectively, which were greater than the minimum required sample sizes.

CT Examination

Triple-phase CT-enhanced images were obtained using a 64-slice CT scanner (Discovery CT750 HD, GE Healthcare, Boston, MA, USA). The scanning parameters were as follows: tube voltage, 120 kV; tube current automatic adjustment technology; scanning range, 500.00 mm; scanning thickness, 1.25 mm; rotation speed, 0.6 s/circle; and matrix size, 512 x 512. The patients were injected with 100 mL of a contrast medium (iohexol; Omnipaque, 300 mg iodine/mL, GE Healthcare) via an elbow vein using a high-pressure syringe (Missouri XD2001, Ulrich Medical, Ulm, Germany) at the rate of 4.5 mL/s. A corticomedullary phase

scan was performed 25–30 seconds after the injection of the contrast medium; the nephrographic scan was performed at 60–70 seconds; and the excretory phase was scanned at 2–3 minutes. All patients were scanned while they were holding their breath after deep inhalation.

Figure 2 shows the radiomics workflow, which included the feature extraction after the CT imaging, which was followed by analysis and signature building.

Feature Extraction

Traditional Feature Extraction

The traditional features included both qualitative and quantitative features. The qualitative features were as follows: side, defined by the location of the tumor in the left or right kidney; location, defined by the location of the tumor in the upper pole, lower pole, or the interpolar region of the kidney; artery_{Intratumoral}, classified as “presence” when tortuous arteries were observed within the renal mass in the corticomedullary phase, and conversely classified as “absence,” as shown in Figure 3A; peritumoral neovascularity, defined by the presence of a blood-supplying artery around the tumor in the corticomedullary phase, as shown in Figure 3B; calcification, defined by the presence of calcification in the tumor; completeness of the pseudocapsule, defined by the presence of a complete, high- or low-attenuation rim surrounding the renal neoplasm in the coronal or sagittal planes for the nephrographic or excretory

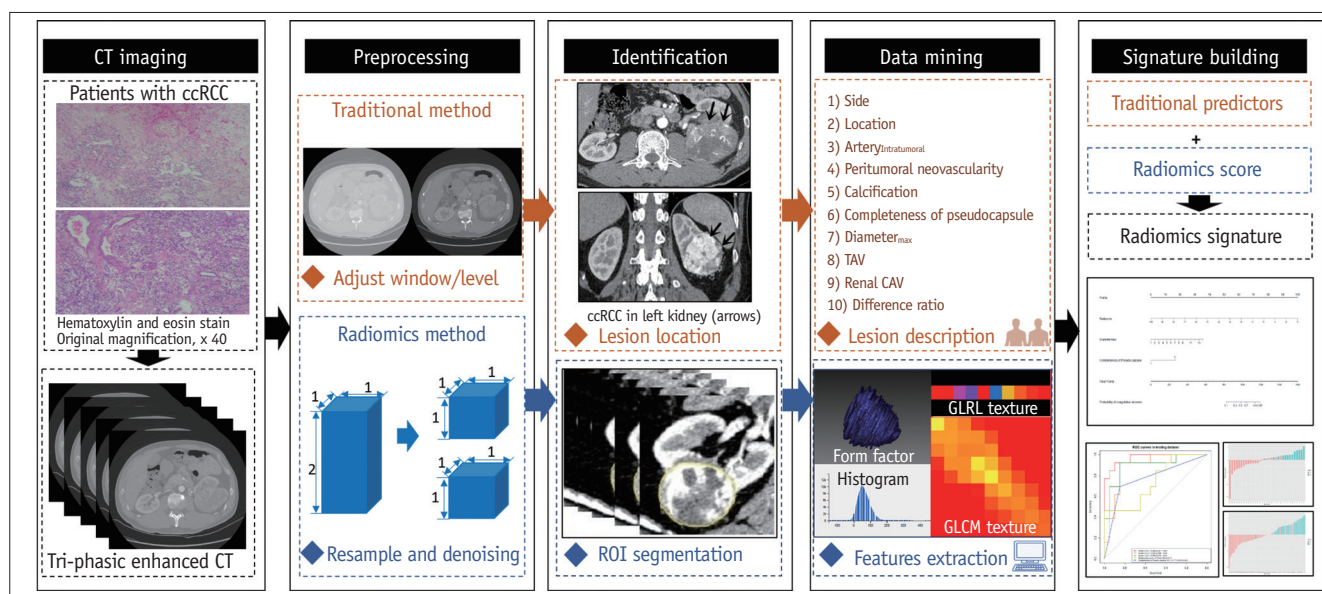


Fig. 2. Flowchart showing process for development of radiomics signature. CAV = cortex attenuation value, GLCM = grey level co-occurrence matrix, GLRL = grey level run-length, ROI = region of interest, TAV = tumor attenuation value

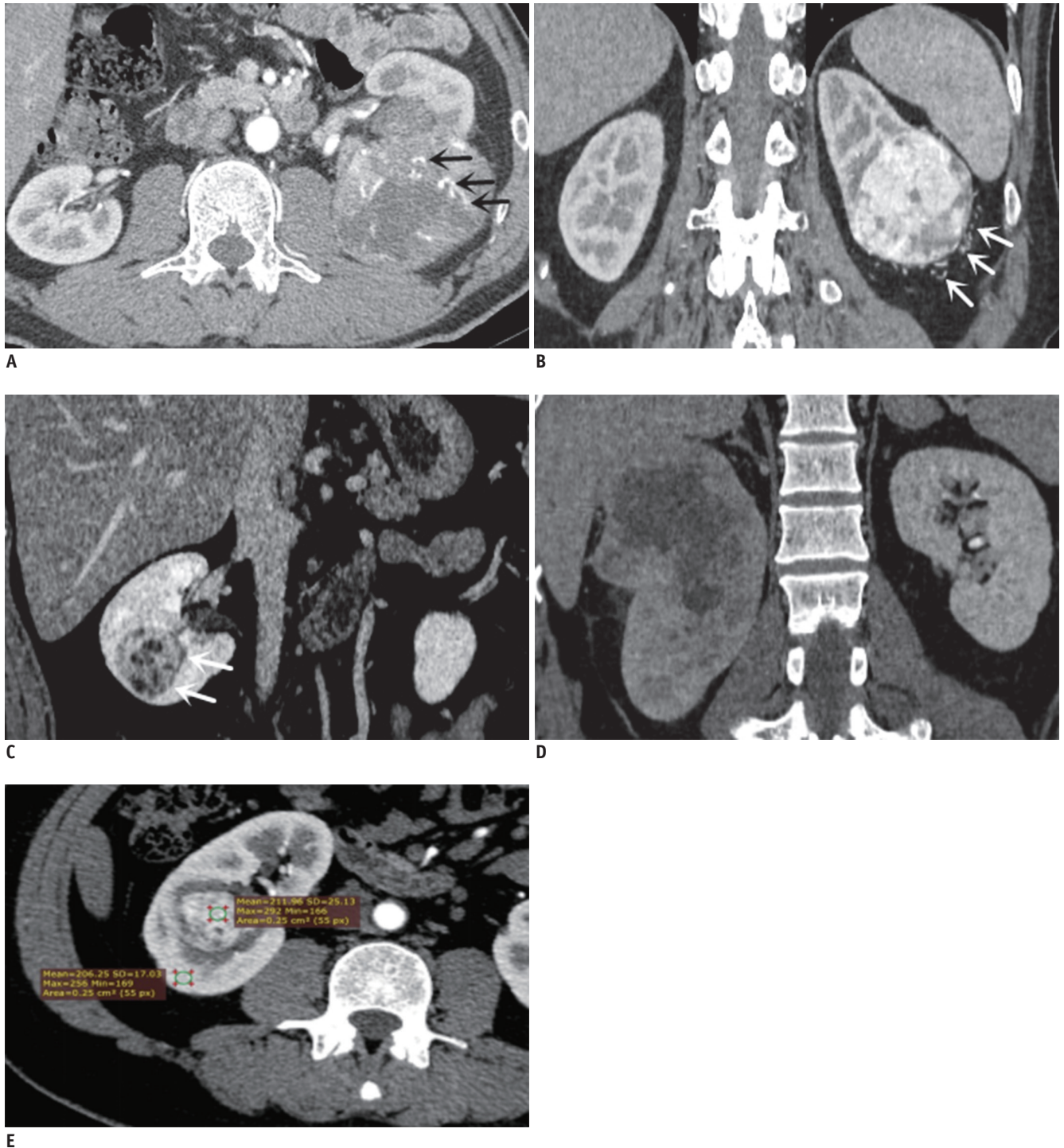


Fig. 3. Image features of artery_{Intratumoral}, peritumoral neovascularity, and complete and incomplete pseudocapsules in patients with ccRCC, and methods for measuring TAV and CAV.

A. Transverse images of corticomedullary phase acquired in 54-year-old woman. Artery_{Intratumoral} was classified as “presence” when tortuous arteries (arrows) were observed within renal mass. **B.** Coronal images of corticomedullary phase acquired in 62-year-old woman. Peritumoral neovascularity was classified as “presence” when tortuous arteries (arrows) were observed around renal mass. **C.** Coronal images of nephrographic phase acquired in 48-year-old man. Completeness of pseudocapsule was classified as “presence” when there was regular, complete low-attenuation rim (arrows) surrounding renal neoplasm. **D.** Coronal images of nephrographic phase acquired in 51-year-old man. Completeness of pseudocapsule was classified as “absence” when there was no clear interface between renal mass and renal parenchyma. **E.** Transverse images of corticomedullary phase acquired in 48-year-old man. TAV and CAV were measured in ROI measuring approximately 25 mm² in most obvious enhancement area of tumor and at same level of renal cortex (oval), respectively.

phase (23), as shown in Figure 3C and D. The quantitative features included diameter_{max}, the tumor attenuation value (TAV), the renal cortex attenuation value (CAV), and the difference ratio. Diameter_{max} was defined as the longest diameter of the largest layer of the tumor in the transverse planes; TAV and CAV were defined as the attenuation of areas with the most obvious enhancement in the tumor and the renal cortex on the same plane, respectively. The difference ratio was defined as the ratio of the difference between TAV and CAV to the renal CAV. These quantitative feature data were obtained in the corticomedullary phase. TAV and CAV were measured by drawing the region of interest (ROI) with a size of approximately 25 mm² in the most obvious enhancement area of the tumor and the same level of the renal cortex, respectively (Fig. 3E). All the measurements and evaluations were conducted by two independent radiologists with 8 (reader 1) or 6 years (reader 2) of experience in abdominal CT interpretation, who were blinded to the pathological results. Among the two sets of findings, the image analysis results obtained by the radiologist with 8 years of diagnostic experience was used for data analysis in this study. The above image analysis processes were performed on the Picture Archiving and Communication System viewer.

Radiomics Feature Extraction

First, data preprocessing was performed to address the differences in image quality and image noise between images and to ensure that image features were calculated using the same specifications. All the images were resampled into voxel sizes of 1 × 1 × 1 mm³ using linear interpolation. In addition, a Gaussian filter was used for denoising. Then, tumor segmentation and feature extraction were performed.

The CT images were stored in the Digital Imaging and Communications in Medicine format and uploaded to the ITK-SNAP software (<http://www.itk-snap.org/>) for three-dimensional manual segmentation of the ROIs. The entire tumor was manually segmented by an abdominal radiologist with 8 years of experience (reader 1). Then, the CT images and ROIs of the patients in this experiment were imported into the Artificial Intelligence Kit (A.K.) software (A.K., GE Healthcare). Next, 385 features based on the individual pixel values in the CT images were automatically extracted. The details of the 385 radiomics features are shown in Figure 4. During these procedures, readers were blinded to all the clinical, pathological, and imaging findings.

Pathological Assessment

Whole-tumor specimens were placed in formalin solution and sent to a pathology laboratory. After staining with

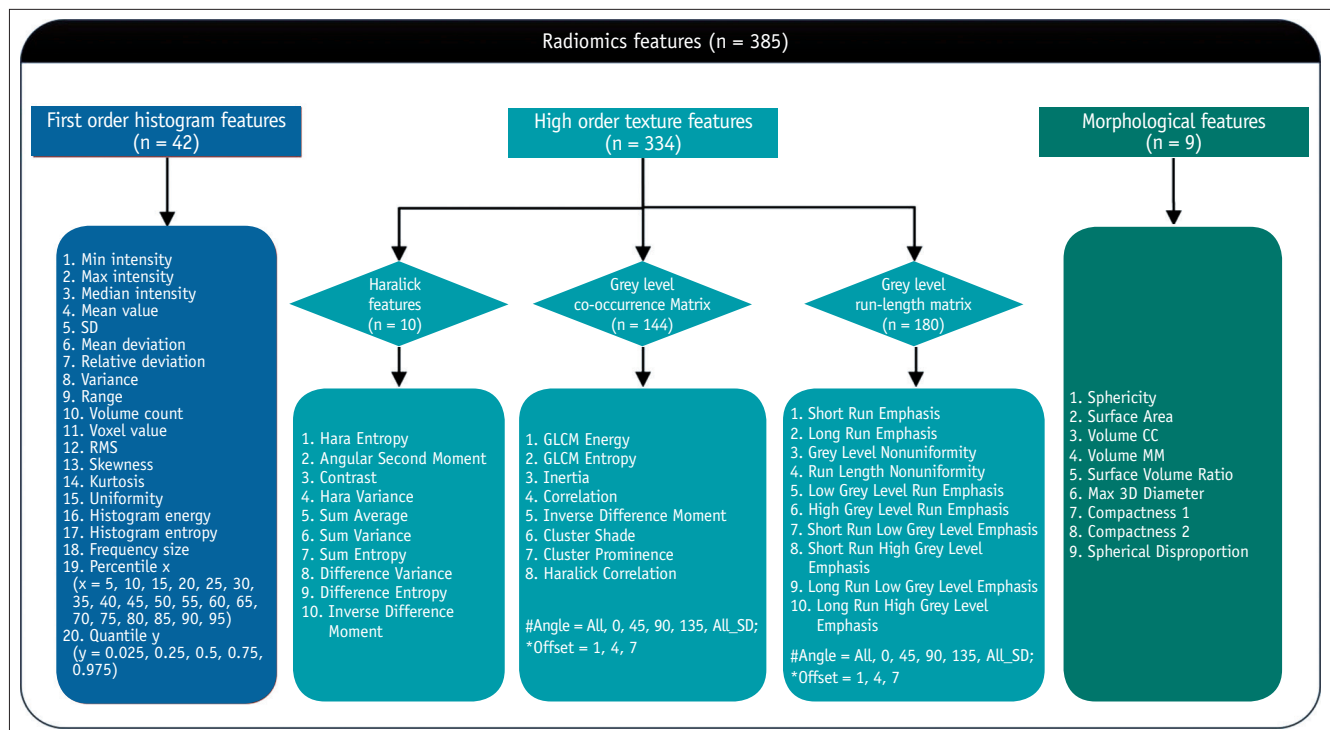


Fig. 4. Details of 385 radiomics features. CC = cm x cm x cm, MM = mm x mm x mm, SD = standard deviation, 3D = three-dimensional

hematoxylin and eosin, a histopathological evaluation of the specimens was performed by a pathologist with more than 10 years of experience, who observed the microscopic CN inside the tumor under a microscope. Pathological images of tumors with and without CN are shown in Figure 5.

Consistency Test

Inter-observer agreement was determined to assess traditional features. We used the intraclass correlation coefficient (ICC). An ICC value > 0.75 was considered indicative of good agreement.

For radiomics features, we randomly selected image data from 20 patients, of which 10 had CN in the tumor. The VOI was delineated by another abdominal radiologist with 6 years of CT interpretation experience (reader 2), and the data were acquired. Finally, the same methods and standards were used to assess the consistency of traditional features.

Statistical Analysis

The categorical variables were compared using the chi-squared test, and the continuous variables were compared using the Mann–Whitney U test. Binary logistic regression analysis was used to analyze the correlation between traditional features and CN.

The least absolute shrinkage and selection operator (LASSO) algorithm was used to identify the best radiomics features that were significantly associated with CN in the ccRCC. A multivariate logical regression model combining the candidate variables selected by the LASSO algorithm was built to ensure efficiency.

An receiver operating characteristic (ROC) curve analysis was used to illustrate the prediction performance of the selected features. The optimal cutoff value was selected as the point when the sensitivity plus specificity was maximal, and the area under the ROC curve (AUC) value was calculated. The DeLong test was used as a difference test on the AUC of different results.

The Mann–Whitney U test, chi-squared test, ICC calculation, and the kappa test were performed using SPSS Statistics (version 22.0, IBM Corp., Armonk, NY, USA). The confidence level was maintained at 95%, and a *p* value of less than 0.05 was considered significant. The DeLong test, LASSO algorithm, multivariate logical regression model construction, and ROC analyses were performed using R Studio (Version 1.0.143© 2009–2016, R Studio, Inc.: <https://www.r-project.org/>). When the Z value was > 1.96 and the *p* value was less than 0.05, the difference between the two groups was considered statistically significant.

RESULTS

The patients were divided into training and validation sets based on the principle of random allocation. The training and validation sets were also analyzed for data pertaining to patient characteristics and traditional and radiomics features.

Patient Characteristics

Using random allocation, 72 patients (48 men, 24 women; mean age, 57.0 ± 8.3 years) were assigned to the training

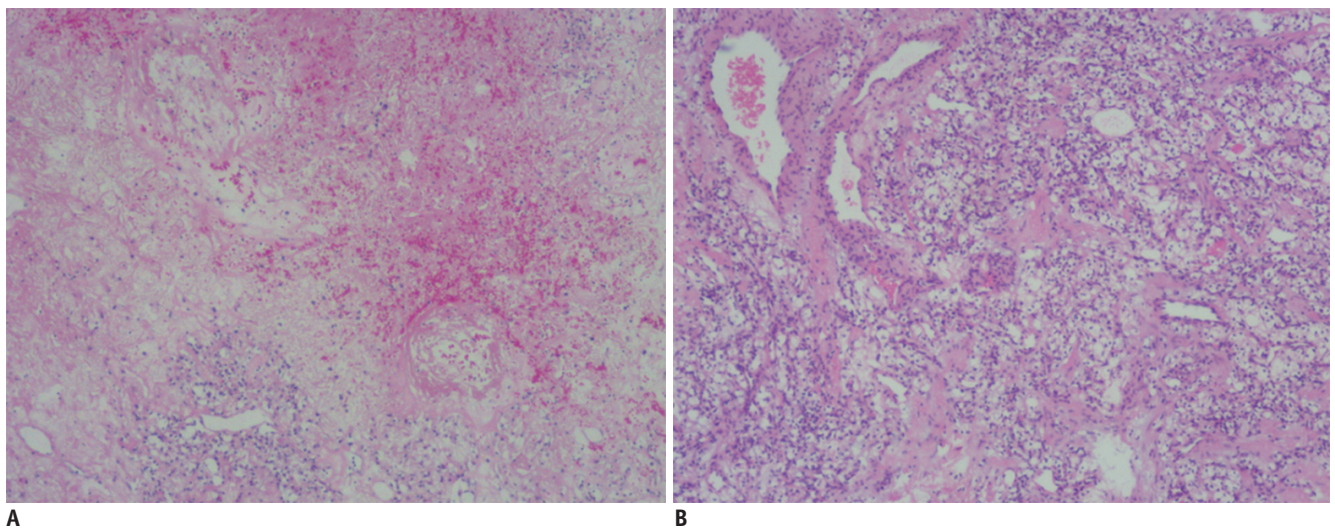


Fig. 5. Photomicrographs (hematoxylin and eosin stain, original magnification, x 40) illustrating coagulative necrosis in ccRCC. A. Low-power magnification view showing coagulative necrosis in ccRCC. **B.** There was no coagulative necrosis in ccRCC.

group, while 33 patients (27 men, 6 women; mean age, 54.3 ± 9.7 years) were allocated to the validation group. The training and validation sets contained 28 and 13 patients with CN in their tumors, respectively. There was no significant intergroup difference in the age and sex of the patients with and without CN in the training and validation sets. However, significant differences were observed in the International Society of Urological Pathology (ISUP) grade, pathology of tumor (pT) stage, and the existence of intratumoral CN in the training and validation sets. CN was more likely to occur in tumors with higher pT stage and ISUP grade in this study. An analysis of the patient characteristics, pathological features, and CN in the training and validation sets is shown in Table 1.

Performance of the Traditional Predictors

Among traditional features, a significant difference between ccRCCs with and without CN was found for two features—diameter_{max} and completeness of the pseudocapsule—with all *p* values < 0.05 in the training and validation sets. The AUC values were 0.713 (95% confidence interval [CI], 0.594–0.833) and 0.760 (95% CI, 0.639–0.880) for diameter_{max} and 0.738 (95% CI, 0.563–0.914) and 0.771 (95% CI, 0.595–0.947) for completeness of the pseudocapsule in the training and validation sets, respectively. No significant difference was observed in the two features among tumors regardless of the presence or absence of CN (all, *p* > 0.05). In the

validation set, besides these two features, significant differences were found for TAV and CAV. Among these four features, the ROC curve for the complete pseudocapsule had the highest AUC value in the two sets. A comparison of the ROC analysis of the imaging features is shown in Tables 2 and 3. We used logistic regression to analyze the correlation between traditional features and CN in the training and validation sets. We found that diameter_{max} and completeness of the pseudocapsule were the only two selected features in the training and validation sets. There were significant differences between the two features and the existence of intratumoral CN. When there was no clear complete pseudocapsule in the ccRCC, the incidence of intratumoral CN was about 11 and 13 times that observed in cases with a clear pseudoenveloped tumor in the training and validation sets, respectively. Moreover, the incidence of CN in the tumor increased by 40% and 80%, respectively, in the two sets when the diameter_{max} of the tumor increased by 1 cm.

A higher AUC value was obtained when the two traditional features (diameter_{max} and completeness of pseudocapsule) were combined by a computational model (Model 1) constructed using multivariate logical regression analysis. The calculation formula for Model 1 is as follows:

$$\text{Model 1 (traditional)} = -5.673 + (0.310 \times \text{diameter max} + 2.317 \times \text{pseudocapsule}).$$

The AUC value was 0.843 (95% CI, 0.750–0.935);

Table 1. Comparison of Patient or Pathological Characteristics by Coagulative Necrosis in Training and Validation Sets

Patient or Pathological Characteristics	Training Set			Validation Set		
	Coagulative Necrosis		<i>P</i>	Coagulative Necrosis		<i>P</i>
	Yes (n = 28)	No (n = 44)		Yes (n = 13)	No (n = 20)	
Sex, No.			0.231			0.737
Male	21 (75.0)	27 (61.4)		11 (84.6)	16 (80.0)	
Female	7 (25.0)	17 (38.6)		2 (15.4)	4 (20.0)	
Age, median (25%, 75%)	55.5 (50.3, 64.0)	56.0 (50.3, 61.8)	0.737	56.0 (51.5, 63.0)	50.5 (46.3, 58.5)	0.065
ISUP grade, No.			0.020*			< 0.001*
Grade I	1 (3.6)	11 (25.0)		0 (0)	7 (35.0)	
Grade II	16 (57.1)	23 (52.2)		7 (53.8)	13 (65.0)	
Grade III	9 (32.2)	9 (20.5)		4 (30.8)	0 (0)	
Grade IV	2 (7.1)	1 (2.3)		2 (15.4)	0 (0)	
pT stage, No.			0.005*			0.040*
pT1	14 (50.0)	35 (79.5)		7 (53.8)	17 (85.0)	
pT2	10 (35.7)	9 (20.5)		4 (30.8)	3 (15.0)	
pT3	4 (14.3)	0 (0)		2 (15.4)	0 (0)	
pT4	0 (0)	0 (0)		0 (0)	0 (0)	

Data in parentheses are percentage. **p* value is less than 0.05. ISUP = International Society of Urological Pathology, pT = pathology of tumor

Table 2. Comparison of ROC Analysis of Imaging Features by Coagulative Necrosis in Training Set

Imaging Features	Coagulative Necrosis		SENS	SPEC	Cut-Off	Youden Index	AUC (95% CI)*	P	Kappa/ICC
	Yes (n = 28)	No (n = 44)							
Side, left/right	15/13	24/20	0.464	0.545	-	0.009	0.505 (0.367–0.643)	0.945	1
Location, upper/middle/lower parts	8/10/10	15/16/13	0.357	0.705	-	0.062	0.540 (0.402–0.677)	0.571	0.894
Artery _{Intratumoral} , No.	28 (100)	38 (86.4)	0.136	1.000	-	0.136	0.568 (0.435–0.701)	0.332	1
Peritumoral neovascularity, No.	15 (53.6)	15 (34.1)	0.659	0.536	-	0.195	0.597 (0.462–0.733)	0.166	0.891
Calcification, No.	7 (25.0)	3 (6.8)	0.932	0.250	-	0.182	0.591 (0.452–0.730)	0.196	1
Completeness of pseudocapsule, No.	9 (32.1)	37 (84.1)	0.679	0.841	-	0.520	0.760 (0.639–0.880)	0.001*	0.775
Diameter _{max} , mean ± SD	7.408 ± 2.532	5.381 ± 2.342	0.714	0.636	5.79	0.350	0.713 (0.594–0.833)	0.002*	0.990
TAV (HU), mean ± SD	176.250 ± 63.464	189.045 ± 56.335	0.386	0.821	218.50	0.207	0.593 (0.455–0.731)	0.184	0.927
CAV (HU), mean ± SD	152.286 ± 33.027	153.795 ± 32.055	0.545	0.607	155.50	0.152	0.540 (0.403–0.678)	0.567	0.894
Difference ratio, mean ± SD	0.186 ± 0.455	0.225 ± 0.367	0.659	0.643	0.18	0.302	0.612 (0.472–0.752)	0.112	0.852
Model 1: traditional predictors, median (25%, 75%)	0.663 (-0.406, 1.612)	-1.624 (-2.177, -0.772)	0.821	0.773	-	-	0.843 (0.750–0.935)	-	-
Model 2: radiomics score, median (25%, 75%)	0.723 (-0.251, 1.178)	-1.880 (-3.310, -0.630)	0.893	0.750	-	-	0.855 (0.770–0.940)	-	-
Model 3: radiomics signature, median (25%, 75%)	1.667 (0.965, 3.237)	-3.010 (-4.050, -1.650)	0.964	0.841	-	-	0.942 (0.890–0.993)	-	-

Data in parentheses are percentage. **p* value is less than 0.05. AUC = area under ROC curve, CAV = cortex attenuation value, CI = confidence interval, ICC = intraclass correlation coefficient, ROC = receiver operating characteristic, SD = standard deviation, SENS = sensitivity, SPEC = specificity, TAV = tumor attenuation value

sensitivity, 0.821 and specificity, 0.773) in the training set, and 0.858 (95% CI, 0.718–0.998; sensitivity, 0.692 and specificity, 0.750) in the validation set. It was higher than the AUC of diameter_{max} and the completeness of the pseudocapsule (all, *p* < 0.05). Moreover, there was no significant difference in other features observed among tumors regardless of the presence or absence of CN (all, *p* > 0.05).

The consistency test results for the traditional features were good (all, > 0.750), and were in the range of 0.775–1.000. The specific results for each traditional feature are shown in Table 2.

Performance of the Radiomics Score

Seven optimal features, called ClusterProminence_{angle90_offset7}, ClusterShade_{angle0_offset7}, Compactness2, HaralickCorrelation_{angle135_offset7}, Inertia_{AllDirection_offset1_SD}, LongRunLowGreyLevelEmphasis_{angle0_offset7}, and

ShortRunEmphasis_{angle45_offset7}, were screened using the LASSO algorithm. The introduction and equations for the seven optimal features are attached in Supplementary Materials.

The multivariate logical regression model (Model 2) built with the seven radiomics features was called the “radiomics score.” The calculation formula for this score is as follows:

$$\text{Model 2 (radiomics score)} = 1.06 \times 10^2 + (-7.98 \times 10 - 8 \times \text{ClusterProminence}_{\text{angle90_offset7}} + 3.14 \times 10 - 5 \times \text{ClusterShade}_{\text{angle0_offset7}} + 5.66 \times 10 - 1 \times \text{Compactness2} + 2.7 \times 10 - 9 \times \text{HaralickCorrelation}_{\text{angle135_offset7}} - 8.31 \times 10 - \text{xInertia}_{\text{AllDirection_offset1_SD}} - 7.65 \times 10^2 \times \text{LongRunLowGreyLevelEmphasis}_{\text{angle0_offset7}} - 1.15 \times 10^2 \times \text{ShortRunEmphasis}_{\text{angle45_offset7}}).$$

The ROC curves constructed using the model had a high AUC value. The AUCs in the training and validation sets were

0.855 (95% CI, 0.770–0.940; sensitivity, 0.893; specificity, 0.750) and 0.885 (95% CI, 0.766–1.000; sensitivity, 0.923; specificity, 0.800), respectively.

The consistency test results for these seven radiomics features were good (all, > 0.750). Among these, the ICC result for Inertia_AllDirection_offset1_SD was the smallest,

Table 3. Comparison of ROC Analysis of Imaging Features by Coagulative Necrosis in Validation Set

Imaging Features	Coagulative Necrosis		SENS	SPEC	Cut-Off	Youden Index	AUC (95% CI)*	P	Kappa/ICC
	Yes (n = 13)	No (n = 20)							
Side, left/right	5/8	12/8	0.615	0.600	-	0.215	0.608 (0.408–0.807)	0.302	1
Location, upper/middle/lower parts	4/7/2	1/11/8	0.950	0.308	-	0.258	0.694 (0.507–0.882)	0.063	0.894
Artery _{intratumoral} , No.	12 (92.3)	18 (90.0)	0.100	0.923	-	0.023	0.512 (0.308–0.715)	0.912	1
Peritumoral neovascularity, No.	6 (46.2)	7 (35.0)	0.650	0.462	-	0.112	0.556 (0.352–0.760)	0.593	0.891
Calcification, No.	0 (0)	3 (15.0)	1.000	0.150	-	0.150	0.575 (0.378–0.772)	0.472	1
Completeness of pseudocapsule, No.	4 (30.8)	17 (85.0)	0.692	0.850	-	0.542	0.771 (0.595–0.947)	0.009*	0.775
Diameter _{max} , mean ± SD	7.284 ± 2.008	5.175 ± 1.917	0.462	1.000	8.725	0.462	0.738 (0.563–0.914)	0.022*	0.990
TAV (HU), mean ± SD	143.154 ± 46.108	186.050 ± 55.376	0.500	0.923	196.500	0.423	0.725 (0.554–0.896)	0.031*	0.927
CAV (HU), mean ± SD	130.077 ± 25.663	162.850 ± 40.176	0.750	0.769	140.500	0.519	0.770 (0.610–0.932)	0.009*	0.894
Difference ratio, mean ± SD	0.128 ± 0.395	0.174 ± 0.312	0.700	0.615	0.123	0.315	0.562 (0.343–0.780)	0.556	0.852
Model 1: traditional predictors, median (25%, 75%)	0.744 (-0.490, 0.985)	-1.335 (-2.243, -1.166)	0.692	0.750	-	-	0.858 (0.718–0.998)	-	-
Model 2: radiomics score, median (25%, 75%)	0.383 (-0.465, 0.769)	-1.617 (-3.020, -0.727)	0.923	0.850	-	-	0.885 (0.766–1.000)	-	-
Model 3: radiomics signature, median (25%, 75%)	0.868 (0.520, 2.636)	-2.692 (-4.435, -0.777)	1.000	0.700	-	-	0.969 (0.921–1.000)	-	-

Data in parentheses are percentage. *p value is less than 0.05.

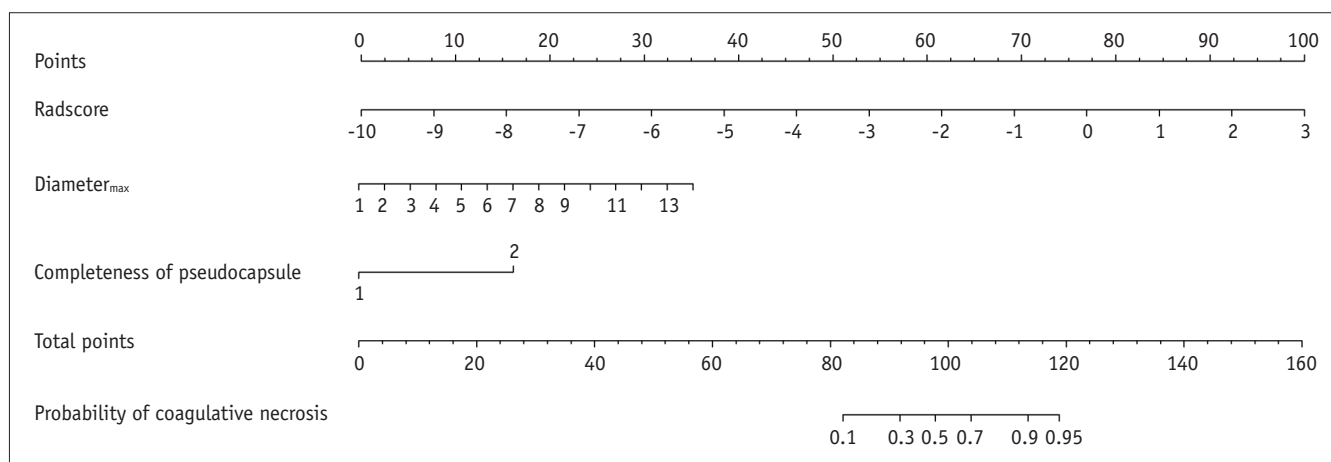
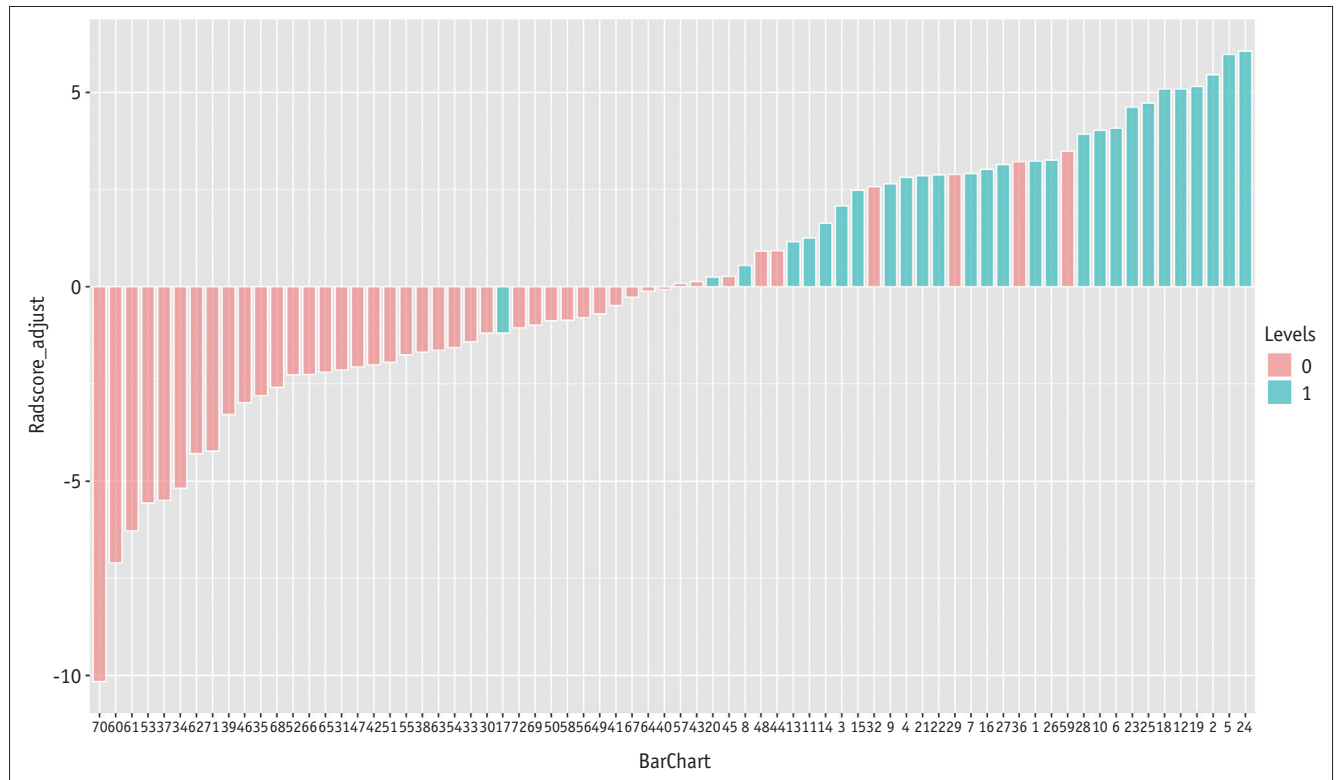
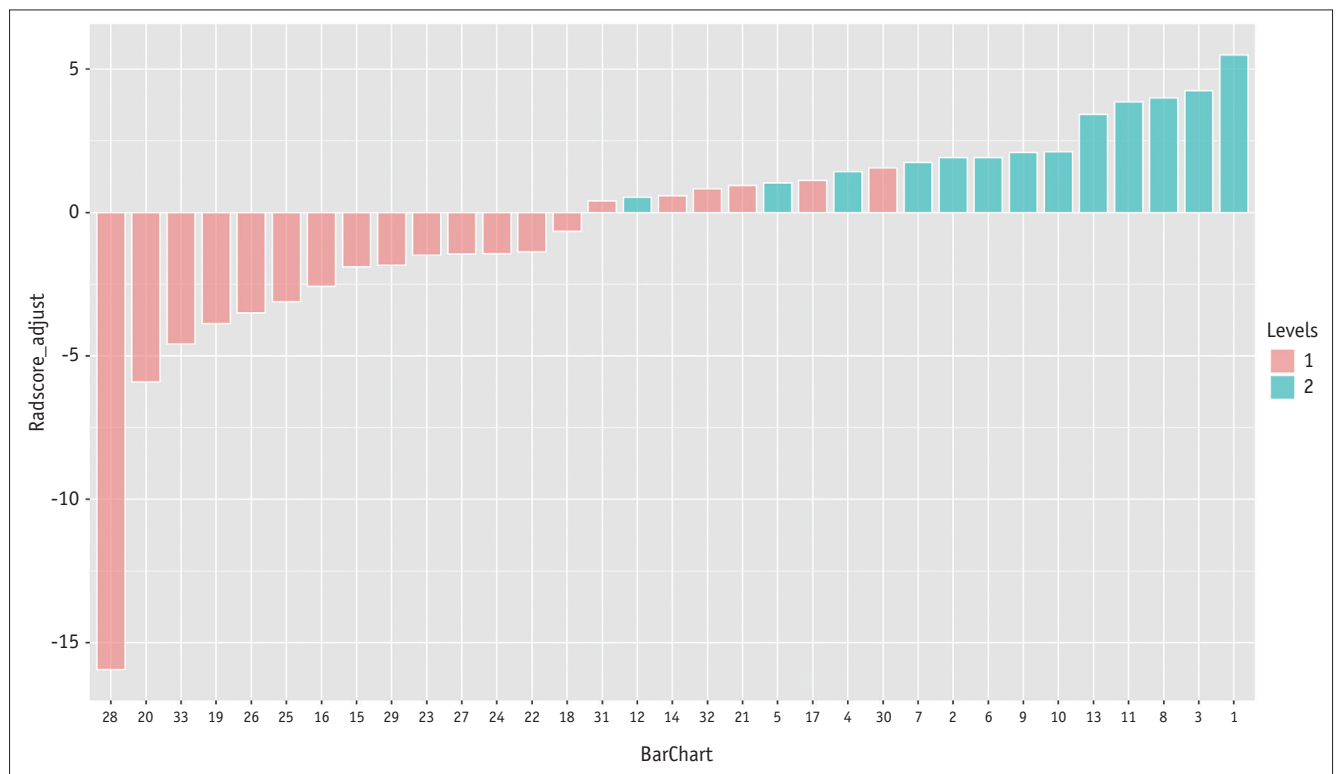


Fig. 6. Nomogram constructed using diameter_{max}, completeness of pseudocapsule and radiomics score. We constructed nomogram of diameter_{max}, with completeness of pseudocapsule and radiomics score serving as predictors for presence of coagulative necrosis within ccRCC. To use nomogram, locate radiomics score calculated by linear formula according to multivariate logical regression model and draw line straight up to points' axis to obtain score associated with radiomics score. Repeat for completeness of pseudocapsule and diameter_{max}. Among these, for characteristics of completeness of pseudocapsule, "1" indicates that pseudocapsule is complete, and "2" indicates that it is incomplete. By summing scores for each point and locating it on total points and drawing line straight down to bottom axis, estimated probability of coagulative necrosis could be determined.



A



B

Fig. 7. BarChart diagram constructed by computational model using radiomics features in training and validation sets.

A. Green part below threshold indicates tumors with coagulative necrosis that are misclassified as non-coagulative necrosis tumors and pink part above threshold represents misclassified data. **B.** Pink part above threshold indicates non-coagulative necrosis tumors misclassified as tumors with coagulative necrosis.

which was 0.91; the result for Compactness 2 was the largest, which was 0.99. The ICC results of the other five features were in the range of 0.91–0.99.

Development of the Radiomics Signature Incorporating Traditional Predictors and Radiomics Score and Performance Assessment

The weighted coefficients of the selected radiomics features in the multivariate logical regression model were presented in a linear formula for radiomics score calculation. A high AUC was obtained with a computational model (Model 3) constructed using the traditional features and the radiomics score. The calculation formula for Model 3 is as follows:

$$\text{Model 3 (nomogram)} = -5.607 + (1.077 \times \text{radiomics score} + 0.382 \times \text{diameter max} + 2.298 \times \text{pseudocapsule}).$$

The AUC was 0.942 and 0.969 in the training and validation sets, respectively. We constructed a nomogram with the diameter_{max}, completeness of the pseudocapsule, and radiomics score as predictors to display the prediction performance of model 3 intuitively. The nomogram is shown in Figure 6.

A BarChart diagram was used to visualize the classification accuracy of model 3 in the training and validation set. The pink and green bars represent tumors with and without CN, respectively. Therefore, the green part below the threshold and the pink part above the threshold are misclassified data. The BarChart diagram of the training group and the validation group is shown in Figure 7.

A comparison of the ROC curves constructed by the two traditional features, Model 1, Model 2, and Model 3 in the training and validation sets is shown in Figure 8.

DISCUSSION

The results of this study showed that CT-based imaging features, irrespective of whether they were traditional or radiomics features, could accurately predict the presence or absence of CN in ccRCC. The results were confirmed further in the analysis of the validation group.

The results of this study indicated that the two artificial recognition features of diameter_{max} and completeness of the pseudocapsule could accurately distinguish between the presence and the absence of CN within the tumor in both training and validation sets. When the two features were

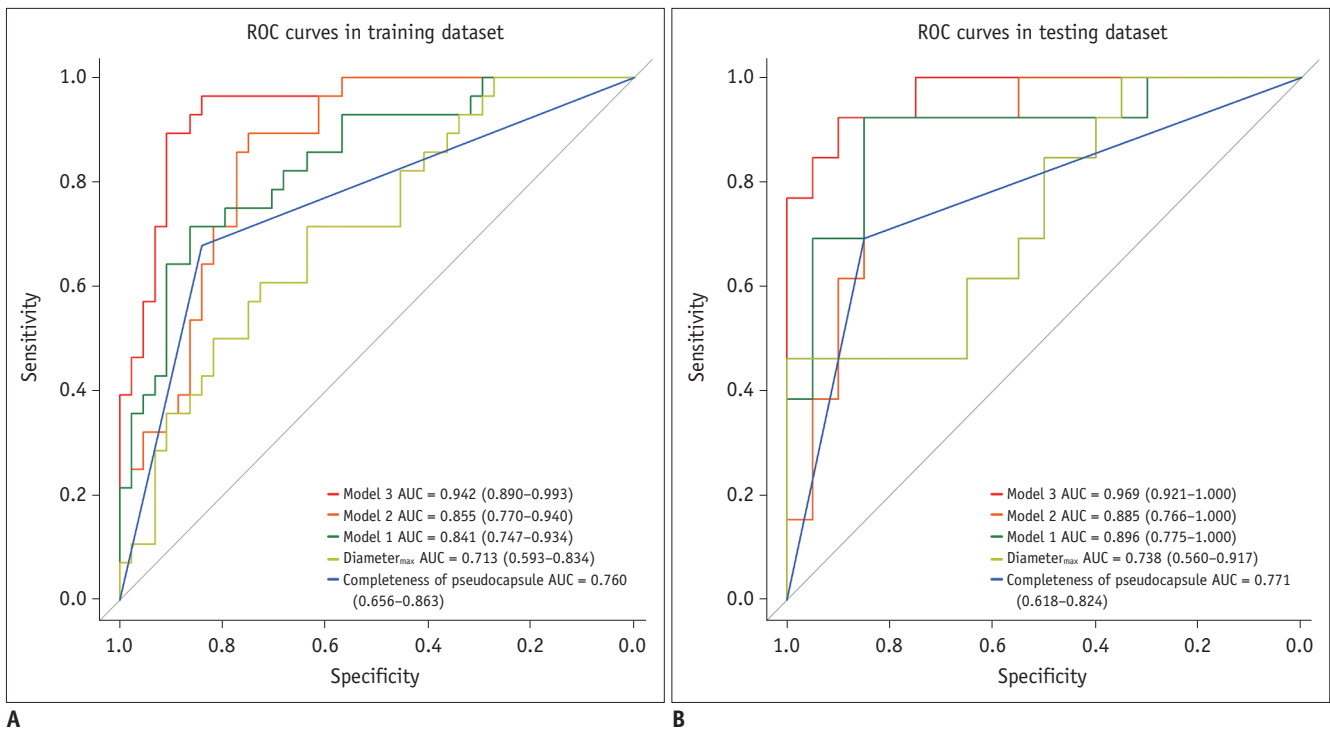


Fig. 8. Comparison of ROC curves constructed by two traditional features, Model 1, Model 2, and Model 3 in training and validation datasets.

A. Comparison of ROC curves constructed by two traditional features, Model 1, Model 2, and Model 3 in training dataset. **B.** Comparison of ROC curves constructed by two traditional features, Model 1, Model 2, and Model 3 in validation dataset. ROC = receiver operating characteristic

combined, a higher AUC could be obtained. The diameter_{max} of the tumor positively correlated with the occurrence of CN, which might be attributed to the greater likelihood of CN within large-diameter tumors (24). In this study, the incidence of coagulation necrosis in ccRCCs increased by 40% and 80% in the training and validation sets, respectively, when the diameter_{max} of the tumor increased by 1 cm. This result is similar to that obtained in previous studies, in which CN was shown to be often present in ccRCCs with size > 10 cm (11). The ROC curves constructed using the feature of completeness of the pseudocapsule had the highest AUC values in the training and validation sets, and its accuracy was higher than that of the other traditional features. This suggested that the completeness of the pseudocapsule was superior in predicting CN in ccRCC. Pseudocapsule formation is a result of tumor growth, which causes compression, ischemia, and necrosis of the adjacent renal parenchyma, and results in the deposition of fibrous tissue (23, 25). Previous pathological studies have shown a higher proportion of CN in ccRCC cases with an incomplete pseudocapsule (25). This conclusion supports the results of our study.

Among the radiomics features, seven quantitative features were selected by the LASSO algorithm to distinguish ccRCC with CN from tumors without CN. The results showed that the multivariate logical regression model constructed using radiomics features was effective in both the training set (AUC, 0.855) and the independent validation set (AUC, 0.885). Radiomics was thus proven to show a high prediction value. Moreover, most of the selected features were texture features, which reflected the heterogeneity of the tumor ROI (21). For example, cluster prominence is a measure of asymmetry of a given distribution, and high values of this feature indicate that the symmetry of the image is low. In this study, the values of cluster prominence extracted from tumors containing CN were higher than the values extracted for tumors without CN. Furthermore, the radiomics features considered in this experiment were extracted based on the whole-tumor delineation on contrast-enhanced CT images. A whole-tumor ROI delineation can reflect more accurately and comprehensively the characteristics and the heterogeneity of the tumor (26, 27). In addition, on contrast-enhanced images, texture features will also reflect the distribution of the contrast agent between the intra- and extravascular extracellular spaces. One hypothesis is that CN results from the tumor's growth beyond the supply of the existing vasculature (28). Therefore, contrast-enhanced images can

more comprehensively reflect the existence of tumor CN.

Moreover, as for traditional features, a higher AUC could be obtained when completeness of the pseudocapsule and diameter_{max} were combined in this study. This indicated that in clinical practice, we could use these traditional features to obtain a preliminary prediction of the presence or absence of CN in a tumor and that doing so would in fact be more convenient and practical than the use of radiomics features. However, evaluation of the traditional features requires experience of image diagnosis, and the results will be influenced by subjective factors. The results for the radiomics features and combined features were slightly higher than those for the traditional features were. Moreover, radiomics features are less affected by subjective factors. However, the entire tumor had to be delineated and specific software was used in the process of analysis; therefore, the process is relatively time- and effort-intensive. This indicated that in clinical practice, if conditions permit, radiomics features could be used to predict CN in ccRCC cases to obtain more accurate results or to evaluate tumors more comprehensively.

In this study, we also analyzed demographic and clinical features. The results indicated that there was no significant difference in demographic characteristics (age and sex) between the ccRCC groups with and without CN, which was consistent with the previous findings (11). Statistically significant differences were found in ISUP grading and pT staging between the ccRCC cases with and without CN. CN in ccRCC was significantly associated with adverse pathologic features, including ISUP grade and pT stage. Moreover, CN was more likely to occur in relatively high-grade and high-stage tumors. This is similar to the results of certain previous studies (11, 29).

The current study had several inherent limitations. First, we only constructed the models using VOIs sketched on the corticomedullary phase CT images and did not extract other phases for the multi-parameter analysis. However, we constructed the ROC curve using the features extracted on the nephrographic phase images in the pre-experimental assessments. The results showed that the AUC value in the nephrographic phase was lower than that in the corticomedullary phase. Second, although our sample size met the standard for a diagnostic experiment after estimation of the sample size, a prospective and multi-center experimental study is still needed for experimental verification of these models in the future.

Overall, according to our current research, the accuracy

of the multivariate logical regression model constructed by combining traditional features and radiomics features in predicting CN in the training and validation sets could reach 0.942 and 0.969, respectively. Thus, imaging methods could be used to assess the prognostic risk of ccRCC to determine which strategy could be used. In addition, the noninvasive nature of the method allowed for repeated evaluations during follow-up and compensated for the limitations of needle biopsies in obtaining accurate findings for CN.

In conclusion, CN in ccRCC could be detected by using traditional features or radiomics features selected based on CT imaging.

Supplementary Materials

The Data Supplement is available with this article at <https://doi.org/10.3348/kjr.2019.0607>.

Conflicts of Interest

The authors have no potential conflicts of interest to disclose.

ORCID iDs

Mengchao Zhang

<https://orcid.org/0000-0002-3733-1597>

Kai Xu

<https://orcid.org/0000-0002-4654-1780>

REFERENCES

- Lane BR, Kattan MW. Predicting outcomes in renal cell carcinoma. *Curr Opin Urol* 2005;15:289-297
- Sheth S, Scatarige JC, Horton KM, Corl FM, Fishman EK. Current concepts in the diagnosis and management of renal cell carcinoma: role of multidetector CT and three-dimensional CT. *Radiographics* 2001;21:S237-S254
- Tsui KH, Shvarts O, Smith RB, Figlin R, de Kernion JB, Belldegrun A. Renal cell carcinoma: prognostic significance of incidentally detected tumors. *J Urol* 2000;163:426-430
- Rabjerg M, Mikkelsen MN, Walter S, Marcussen N. Incidental renal neoplasms: is there a need for routine screening? A Danish single-center epidemiological study. *APMIS* 2014;122:708-714
- Hollingsworth JM, Miller DC, Daignault S, Hollenbeck BK. Rising incidence of small renal masses: a need to reassess treatment effect. *J Natl Cancer Inst* 2006;98:1331-1334
- Leibovich BC, Lohse CM, Crispen PL, Boorjian SA, Thompson RH, Blute ML, et al. Histological subtype is an independent predictor of outcome for patients with renal cell carcinoma. *J Urol* 2010;183:1309-1315
- Delahunt B, Cheville JC, Martignoni G, Humphrey PA, Magi-Galluzzi C, McKenney J, et al. The International Society of Urological Pathology (ISUP) grading system for renal cell carcinoma and other prognostic parameters. *Am J Surg Pathol* 2013;37:1490-1504
- Klatte T, Kroeger N, Zimmermann U, Burchardt M, Belldegrun AS, Pantuck AJ. The contemporary role of ablative treatment approaches in the management of renal cell carcinoma (RCC): focus on radiofrequency ablation (RFA), high-intensity focused ultrasound (HIFU), and cryoablation. *World J Urol* 2014;32:597-605
- Ljungberg B, Cowan NC, Hanbury DC, Hora M, Kuczyk MA, Merseburger AS, et al. EAU guidelines on renal cell carcinoma: the 2010 update. *Eur Urol* 2010;58:398-406
- Amtrup F, Hansen JB, Thybo E. Prognosis in renal carcinoma evaluated from histological criteria. *Scand J Urol Nephrol* 1974;8:198-202
- Sengupta S, Lohse CM, Leibovich BC, Frank I, Thompson RH, Webster WS, et al. Histologic coagulative tumor necrosis as a prognostic indicator of renal cell carcinoma aggressiveness. *Cancer* 2005;104:511-520
- Zhang L, Zha Z, Qu W, Zhao H, Yuan J, Feng Y, et al. Tumor necrosis as a prognostic variable for the clinical outcome in patients with renal cell carcinoma: a systematic review and meta-analysis. *BMC Cancer* 2018;18:870
- Dagher J, Delahunt B, Rioux-Leclercq N, Egevad L, Coughlin G, Dungleison N, et al. Assessment of tumour-associated necrosis provides prognostic information additional to World Health Organization/International Society of Urological Pathology grading for clear cell renal cell carcinoma. *Histopathology* 2019;74:284-290
- Ficarra V, Brunelli M, Novara G, D'Elia C, Segala D, Gardiman M, et al. Accuracy of on-bench biopsies in the evaluation of the histological subtype, grade, and necrosis of renal tumours. *Pathology* 2011;43:149-155
- Mally AD, Gayed B, Averch T, Davies B. The current role of percutaneous biopsy of renal masses. *Can J Urol* 2012;19:6243-6249
- Herts BR, Coll DM, Novick AC, Obuchowski N, Linnell G, Wirth SL, et al. Enhancement characteristics of papillary renal neoplasms revealed on triphasic helical CT of the kidneys. *AJR Am J Roentgenol* 2002;178:367-372
- Choi SY, Sung DJ, Yang KS, Kim KA, Yeom SK, Sim KC, et al. Small (< 4 cm) clear cell renal cell carcinoma: correlation between CT findings and histologic grade. *Abdom Radiol (NY)* 2016;41:1160-1169
- Lambin P, Rios-Velazquez E, Leijenaar R, Carvalho S, van Stiphout RG, Granton P, et al. Radiomics: extracting more information from medical images using advanced feature analysis. *Eur J Cancer* 2012;48:441-446
- Ding J, Xing Z, Jiang Z, Chen J, Pan L, Qiu J, et al. CT-based radiomic model predicts high grade of clear cell renal cell carcinoma. *Eur J Radiol* 2018;103:51-56

20. Zhang X, Xu X, Tian Q, Li B, Wu Y, Yang Z, et al. Radiomics assessment of bladder cancer grade using texture features from diffusion-weighted imaging. *J Magn Reson Imaging* 2017;46:1281-1288
21. Zhu X, Dong D, Chen Z, Fang M, Zhang L, Song J, et al. Radiomic signature as a diagnostic factor for histologic subtype classification of non-small cell lung cancer. *Eur Radiol* 2018;28:2772-2778
22. Smyth EC, Verheij M, Allum W, Cunningham D, Cervantes A, Arnold D, et al. Gastric cancer: ESMO clinical practice guidelines for diagnosis, treatment and follow-up. *Ann Oncol* 2016;27:v38-v49
23. Tsili AC, Argyropoulou MI, Gousia A, Kalef-Ezra J, Sofikitis N, Malamou-Mitsi V, et al. Renal cell carcinoma: value of multiphase MDCT with multiplanar reformations in the detection of pseudocapsule. *AJR Am J Roentgenol* 2012;199:379-386
24. Schiavina R, Borghesi M, Chessa F, Dababneh H, Bianchi L, Della Mora L, et al. The prognostic impact of tumor size on cancer-specific and overall survival among patients with pathologic T3a renal cell carcinoma. *Clin Genitourin Cancer* 2015;13:e235-e241
25. Cho S, Lee JH, Jeon SH, Park J, Lee SH, Kim CH, et al. A prospective, multicenter analysis of pseudocapsule characteristics: do all stages of renal cell carcinoma have complete pseudocapsules? *Urol Oncol* 2017;35:370-378
26. Ng F, Ganeshan B, Kozarski R, Miles KA, Goh V. Assessment of primary colorectal cancer heterogeneity by using whole-tumor texture analysis: contrast-enhanced CT texture as a biomarker of 5-year survival. *Radiology* 2013;266:177-184
27. Ng F, Kozarski R, Ganeshan B, Goh V. Assessment of tumor heterogeneity by CT texture analysis: can the largest cross-sectional area be used as an alternative to whole tumor analysis? *Eur J Radiol* 2013;82:342-348
28. Brinker DA, Amin MB, de Peralta-Venturina M, Reuter V, Chan DY, Epstein JI. Extensively necrotic cystic renal cell carcinoma: a clinicopathologic study with comparison to other cystic and necrotic renal cancers. *Am J Surg Pathol* 2000;24:988-995
29. Khor LY, Dhakal HP, Jia X, Reynolds JP, McKenney JK, Rini BI, et al. Tumor necrosis adds prognostically significant information to grade in clear cell renal cell carcinoma: a study of 842 consecutive cases from a single institution. *Am J Surg Pathol* 2016;40:1224-1231